



HAL
open science

Far-field plume properties of a cluster of 100 W-class permanent magnets Hall thrusters

T Hallouin, A Guglielmi, A Gurciullo, B Moriconi, S Mazouffre

► **To cite this version:**

T Hallouin, A Guglielmi, A Gurciullo, B Moriconi, S Mazouffre. Far-field plume properties of a cluster of 100 W-class permanent magnets Hall thrusters. 37th International Electric Propulsion Conference, Jun 2022, Cambridge, United States. hal-03797516

HAL Id: hal-03797516

<https://hal.science/hal-03797516v1>

Submitted on 4 Oct 2022

HAL is a multi-disciplinary open access archive for the deposit and dissemination of scientific research documents, whether they are published or not. The documents may come from teaching and research institutions in France or abroad, or from public or private research centers.

L'archive ouverte pluridisciplinaire **HAL**, est destinée au dépôt et à la diffusion de documents scientifiques de niveau recherche, publiés ou non, émanant des établissements d'enseignement et de recherche français ou étrangers, des laboratoires publics ou privés.

Far-field plume properties of a cluster of 100 W-class permanent magnets Hall thrusters

IEPC-2022-292

*Presented at the 37th International Electric Propulsion Conference
Massachusetts Institute of Technology, Cambridge, MA, USA
June 19-23, 2022*

T. Hallouin*, A. Guglielmi † A. Gurciullo‡ B. Moriconi §
Exotrail, Massy, Essone, 91300, France

and

S. Mazouffre¶
Centre National de la Recherche Scientifique, Orléans, Loire, 45000, France

In this study, a cluster of two 100 W-class permanent magnets Hall thrusters is characterized in terms of plasma plume content in the large PIVOINE_2G vacuum chamber. The two thrusters have been operated with xenon as a propellant over a broad range of discharge voltages and mass flow rates, with their own 1 A-class hollow cathode. Plasma plume properties have been measured by means of a Faraday cup, a repulsing potential analyzer for both single thruster and cluster operations over a 180° circular arc. Such measurements have been performed for two different anode spacings. The ion current density angular profiles measured in the plume of a cluster tends to be higher in the core of the plume and lower at larger angles compared to the sum of ion current density angular profiles of two single thrusters. Furthermore, efficiency analysis has revealed interesting features. The beam efficiency appeared to be lower for cluster operation. Also lower performances were found out for the two anode blocks operated in close configurations. The shape of the ion energy distribution functions measured in the plume of a cluster is comparable to the one observed for a single thruster operation. Notwithstanding, the broadening of the main peak appears to be higher for cluster operation, as the interactions between the two plumes favours elastic collisions. Also, the most probable energy remains unchanged in both mode operations while the mean energy of ions remains lower for cluster operation. A cluster of two anode blocks was also operated with a shared cathode. The cathode position clearly affects the cluster parameters by reducing the extracted ionic current and increasing the divergence at 90% (associated to an increasing of CEX) when the cathode-cluster axis distance increases.

*Propulsion Engineer, thibault.hallouin@exotrail.com.

†Research Project Engineer, PhD, alexandre.guglielmi@exotrail.com

‡VP Propulsion, antonio.gurciullo@exotrail.com

§Propulsion Engineer, bruno.moriconi@exotrail.com

¶Research Director, CNRS; Head of EP team, ICARE, stephane.mazouffre@cnrs-orleans.fr.

Nomenclature

η_b	Beam efficiency
I_b	Beam current
$I_{i,tot}$	Total ion current
P_d	Discharge power
U_d	Discharge voltage
d	Discharge channel mean diameter
\dot{m}_a	Anode mass flow
R	Distance between the probe and the exit plane of the thruster

I. Introduction

Over the last decade, the satellite miniaturization has opened up a new space market. Technologically simple, inexpensive and flexible, the nano- and micro-satellites (1 – 200 kg) are well suited for various missions in LEO, such as communication, science and Earth observation. Propulsion systems naturally had to adapt to the new requirements through miniaturization and power consumption reduction. Due to limitations in terms of volume and mass, electric thrusters are better suited for very small satellites compared to their chemical counterpart. Indeed, the high specific impulse (Isp) of EP devices directly translates into a low propellant amount for a given mission profile. There are various types of small low-power electric thruster technologies according to the way thrust and Isp are produced. The thruster collection covers a very broad range of operating parameters that means most micro-satellite mission needs can be satisfied when selecting the proper device. Among all technologies, Hall thrusters (HTs) currently offer the highest thrust density and thrust-to-power ratio.¹ They are therefore well-suited for orbit transfer maneuvers and drag compensation at low altitude. Besides, the combination of multiple Hall thrusters represents an attractive propulsion approach for spacecraft requiring more powerful electric propulsion systems.^{2,3}

To increase power level achievable by an electric propulsion system, different alternative were identified: develop a single thruster head with desired power level or cluster several lower power devices to reach the targeted outcome. Although a single HT has better performances and a lower dry mass compared to an array of thrusters, the clustering was identified as a better candidate since it presents several advantages over the monolithic approach.⁴⁻⁷ The advantages identified and developed below are true for low as well as high power devices.

Thus, the clustering offers a high degree of **flexibility** as it can be used in a very wide range of operating parameters. As the throttleability of the system is expended, a cluster is thus suitable for missions requiring variable propulsive capacities. Furthermore, system **reliability** is improved due to the inherent redundancy of operating multiple devices, providing that the latter are operated independently (i.e. each thruster is operated with its own Power Processing Unit).

Cluster configuration is also **cost** and **time effective** since it does not require the development and the qualification of a HT for the targeted power range. Only subsystems need to be managed to be conformed with multiple HTs operation. Moreover, in the case of very high-power devices (100 kW) development only a few of ground facilities are capable of achieving decent vacuum level. As high power thruster operation lead to an inescapable increase of mass flow rates, the pumping speed capability must be necessary improved. Constructing and operating such facilities can easily be much expensive than the thruster development. Clustering offers here an alternative as each lower-power thruster head can be individually qualified.

Last but not least, clustering is suitable for **thrust vectoring**. During a space mission, the center of mass of the spacecraft changes, owing to both propellant consumption and thermal deformation. Thus, for monolithic thruster operation, the thruster centerline, i.e. the thrust vector, is not aligned anymore with the center of mass of the spacecraft, leading to undersired torques of the satellite. This phenomena can be counterbalanced by thrust vectoring, i.e. by steering the average thrust vector of the propulsive system. Although alternative systems have been suggested, e.g. the use of a gimbal mechanism⁸ or a tilting of the magnetic field to direct the ions beam,⁹ clustering appears as the best candidate for long term operation. Whereas the gimbal mechanism is costly, heavy and not reliable enough in space environment, the thrust steering device increases erosion rate and drastically reduce performances.

It is therefore of interest to measure cluster plume properties to verify whether the clustering has an impact on both plume arrangement and performances. Measurements can be compared to monolithic thruster plume properties to develop analytical methods for predicting cluster operation. In other terms, the model may be able to anticipate performances and plume properties from a single thruster operation. This would represent a valuable gain of time and cost, as only one single thruster could be characterized to predict the full system behavior. Such measurements are also of interest to gain insight on the physical interaction not only between the plumes of each thruster head but also with the surrounding environment, i.e. the spacecraft and particularly the solar panels.

II. Experimental set-up

A. Cluster of low power Hall thruster

1. ISCT100-v2 - 100 W-class Hall thruster

The cluster was composed of the ISCT100v2-ICARE-0X – X referring to the number of the anode block used. The ISCT100v2-ICARE-0X, standing for ICARE Small Customizable Thruster, is a 100 W-class Hall thruster (see Figure 1), with performances comparable to the Busek BHT-100.¹⁰ The ISCT100-v2 corresponds to the $2S_0-2B_0$ configuration presented in Ref. 11 and constitutes an example of a low-power Hall thruster.

The annular discharge channel is made of BN-SiO₂. A non-magnetic stainless-steel ring anode is placed at the back of the discharge channel, against the internal surface of the outer ceramic wall.

The propellant gas is injected homogeneously inside the channel through a mullite disk, of which the high porosity allows for diffusion of the gas. The magnetic field is generated by means of cylindrical permanent magnets, located on both sides of the annular channel. The symmetrical distribution as well as the lense-shape of the magnetic field are provided by a pure iron magnetic circuit. The maximum magnetic amplitude is reached at the channel exit plane, while a near-zero amplitude is reached in the anode area.

Each anode was operated with its own cathode. The Cathode Reference Potential (CRP) is maintained around -10 V by adjusting the heating power to limit instabilities which strongly impact discharge stabilities and thus plume measurements.

2. Cluster configurations

The essence of this study consists in comparing monolithic THD operation to cluster operation. To do so, different configurations were characterized in terms of far-field plume properties to assess how cluster operation impacts the plume arrangement and the operation of a single THD. Far-field plume properties were then measured for :

- A single thruster head (referred herein as X1). In this configuration, the Hall thruster was placed in such a way that the thruster centerline is aligned with the vacuum chamber axis. In other terms, the thruster is centered with respect to the probe axis at the 0 degree position.
- A cluster of two thruster heads with variation of the separated distance between the two thruster axis (referred herein as X2). In such configuration, only the cluster centerline is aligned with the vacuum chamber axis. Note that the thrusters of left- and right-hand sides (in front view) are respectively named as THD1 and THD2. Thus, THD1 and THD2 are respectively in positive and negative angle sides for angular probe measurements. Anode spacing was varied in close and far configurations, referred as X2.A and X2.B configurations, respectively. In the far configuration, the magnetic field of the two thrusters do not interact.

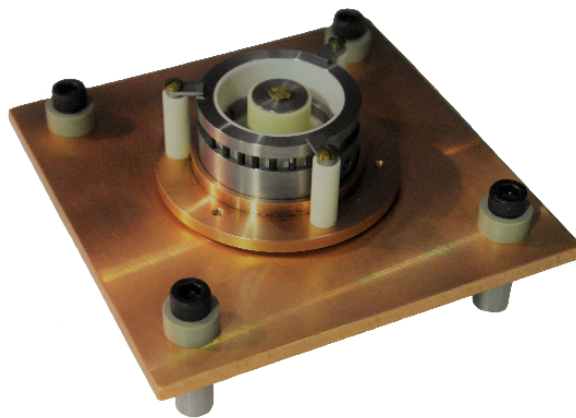


Figure 1: ISCT100v2-ICARE-0X, 100 W-class HT.

- A cluster of two anode blocks with a shared cathode at different positions (referred herein as X2-SC)

Note that the far-field plume properties of a cluster of three independent THDs was also characterized. Results will be presented in a future paper.

The cluster positioning and magnetic field mapping has been characterized at Synchrotron SOLEIL. The magnetic mapping was characterized for a cluster of two anode blocks in the close configuration.

Note that to counterbalance the torque direction of ions imposed by the magnetic field direction, the magnetic field direction was inverted for the two thrusters, i.e. at the inner pole the magnetic field strengths are respectively negative and positive for THD2 and THD1.

The magnetic mapping has shown that the radial magnetic field intensity reaches more than 30% of the maximum magnetic barrier near the cluster axis, due to the proximity of the two anode blocks. That proximity impacts the radial distribution of the magnetic field beyond the exhaust plane of each anode block. The magnetic field lines beyond acceleration channel are also apparently tilted.

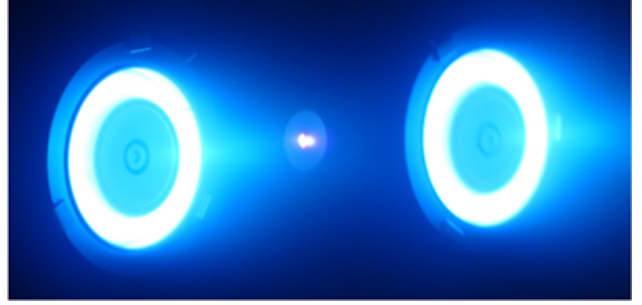


Figure 2: Cluster operating with two anode blocks and a shared cathode.

B. PIVOINE-2g

The PIVOINE-2g – stands for Propulsion Ionique pour les Vols Orbitaux, Interprétations et Nouvelles Expériences - 2ème génération – vacuum chamber is a stainless-steel cylinder tank 4 m in length and 2.2 m in diameter. The chamber is equipped of a 5000 l/s turbomolecular pumps, used to remove light molecular gases (e.g. hydrogen), and two cryogenic stages located at the back of the tank. The first stage is composed of three cryogenic panels sustained at 42 K to efficiently adsorb xenon. Beyond, a large cryo-panel is sustained at 16 K to remove both nitrogen and oxygen. The two stages of cryo-panels are shielded from ion beam by means of water-cooled tilted graphite tiles. The multistage pumping system provides an operating background pressure below 1×10^{-5} mBar – N₂.

The test bench is equipped of a movable arm on which 15 Faraday probes are positioned (see Figure 3) for a complete angular 3D mapping of the ion current in the plume of HTs. The arm can be customized in such a way that extra electrostatic probes can be positioned for 2D measurements over a 240° circular arc. For the far-field plume measurements, both Faraday Cup (FC) and Retarding Potential Analyzer (RPA) positioned along the semi arc of the thruster plane (as shown in Figure 3) were used in addition of the 15 Faraday probes. Designs are detailed in the following sections.

C. Faraday cup

The ion current has been extensively measured in the far-field plume of various power-class Hall thrusters. Such measurements can be performed through various electrostatic probes as nude Faraday probe or planar probe,¹² planar probe with a guard ring or Faraday cup. Innovative design has also been tested to counterbalance the overestimation of the collected current due to both sheath effects and CEX ions collection. In the present study, the ion beam of both single thruster and cluster has been investigated using a Faraday Cup, of which the working principle and the design is described in the following sections.¹³

1. Probe design

A Faraday Cup (FC) is an electrostatic planar probe with an isolated conductive cup. Compared to conventional planar probes, the FC is appropriate for accurately measuring the ion current density in the far-field plume of HT's as its closed geometry prevents from edge effects due to plasma sheath formation.¹³⁻¹⁵ The FC used in the different plume measurements is also described in Ref. 14.

A Faraday cup is composed of key components shown in the cross-section view scheme in Figure 4. The role as the design justification is given in the following section to grasp the overall working principle of the

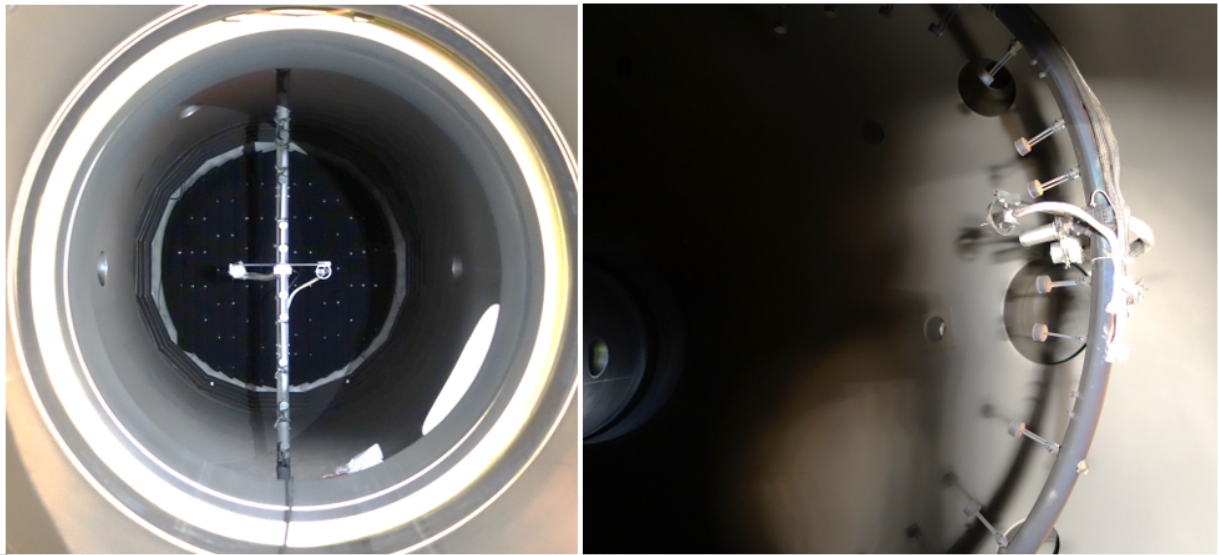


Figure 3: Front view and side view of the 15 Faraday probes, Faraday Cup and Retarding Potential Analyzer used in Pivoine and mounted on a rotary motor (from -120° to $+120^\circ$).

electrostatic probe.

Number (1) refers to the FC aluminum body directly exposed to plasma.

The collimator (2) is used to screen electrons and define the solid angle/ surface collection. Since the FC is placed in a high energy ions beam, the choice of the collimator material is relevant to limit perturbations due to sputtering and secondary electron emission. Thus, the collimator is made of graphite, selected for its low sputtering yield. The orifice diameter must be dimensioned to minimize charge exchange and scattering collisions within the cup due to gas pressure build up. The orifice is set to 10 mm, i.e. the surface for ion current collection is 78.5 mm^2 . The collimator is electrically isolated from the biased cup and the external body using a PEEK spacer (3). Thus, the collimator can be independently biased or floating.

The collector (5) is made of an aluminum foam disk and is mechanically attached to the stainless-steel cylinder (4). The cylinder plus the collector form the cup. The whole volume porosity of the metal foam is $60 \pm 5 \%$. Such structure must prevent perturbation owed to ion bombardment and secondary electron emission. The length of the cup is around 50 mm, long enough to ensure the measurement are insensitive to the local plasma properties, i.e. the space-charge sheath thickness inside the probe.

A grounded and calibrated Keithley 2410 1100 V source-meter instrument has been used to measure the collected current. The unit was operated in voltage source to apply a constant negative bias voltage of -50 V to the probe cup and to read the current.

2. Theory

Faraday Cup measurements can be used to compute the total ion current $I_{i,tot}$ in the beam. Since $R > 10d$ (with R the distance between the thruster exit plane and the probe and d the mean diameter of the discharge channel), the plasma is assumed to originate from a source point. The total ion current, which is equal to

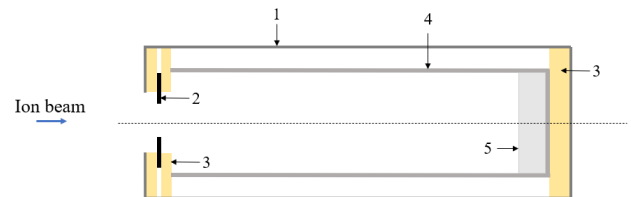


Figure 4: Scheme of the Faraday Cup showing the main elements, namely (1) the aluminum housing, (2) the graphite entrance collimator, (3) the PEEK insulators, (4) the stainless-steel cylinder and (5) the aluminum foam collector.

the integral over an hemisphere of the ion current density j_i therefore reads:¹⁶

$$I_{i,tot} = \int_{-\pi/2}^{\pi/2} \int_{-\pi/2}^{\pi/2} j_i(\theta, \phi) dS. \quad (1)$$

THRUSTER CENTERLINE ALIGNED WITH THE PROBE AXIS AT 0° POSITION (SINGLE THRUSTER CONFIGURATION)

In spherical coordinates, the elementary surface dS is defined by polar and azimuth angles, θ and ϕ , respectively, such as: $dS = R^2 \sin(\theta) d\theta d\phi$. The quantity $j_i(\theta, \phi)$ is not experimentally measured directly. Instead, only $j_i(\theta, 0)$ is probed. We assume the plume properties are symmetrical and isotropic with respect to the thruster axis that is $j_i(\theta) = j_i(\phi)$. We obtain a new equation, which can be solved from FC data:

$$I_{i,tot} = \pi R^2 \int_{\pi}^0 j_i(\theta) \sin(\theta) d\theta. \quad (2)$$

THRUSTER CENTERLINE NOT ALIGNED WITH THE PROBE AXIS AT 0° POSITION

For the cluster configurations, the probe axis is aligned with the cluster centerline, so that the distance

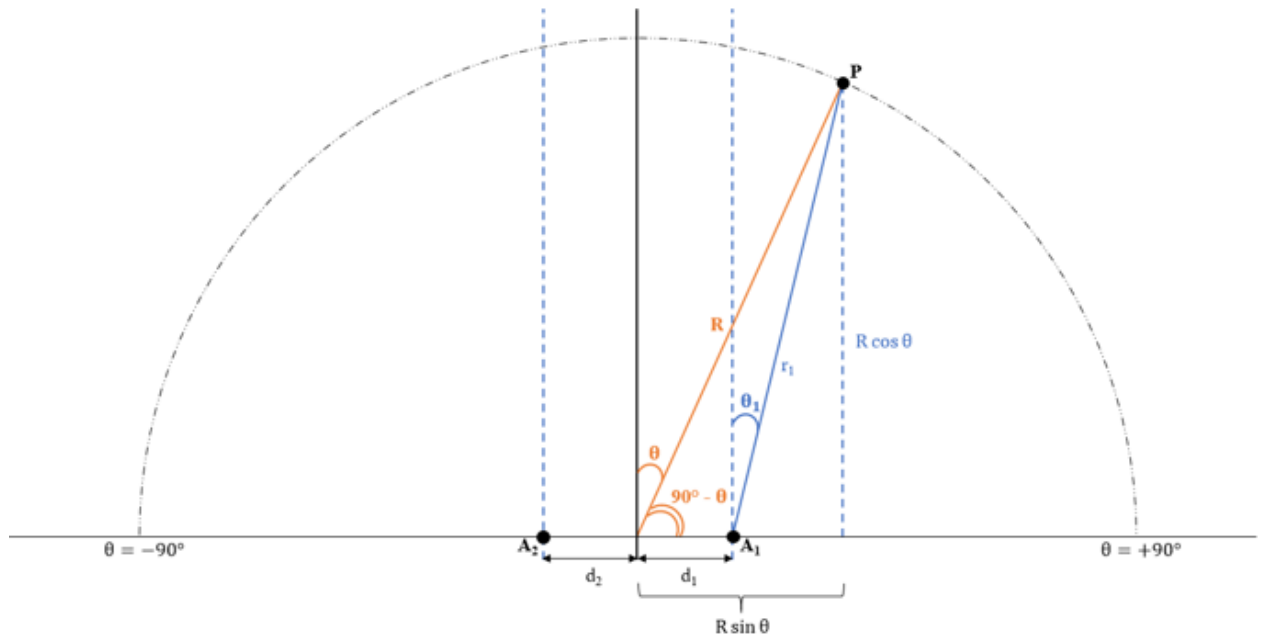


Figure 5: Scheme for thruster centerline not aligned with the probe at 0 degree position.

between the probes and the exit plane varies with θ as illustrated in Figure 5.

A_1 and A_2 respectively represent the thruster locations and are related to plasma source points. P represents the probe location. d_1 and d_2 are the distance between the thrusters and the cluster centerlines. In the course of this study, the two thrusters are set at same distances relative to the cluster centerline, so $d_1 = d_2 = d$. Thus, the distance r_1 between A_1 and the probe therefore reads:

$$r_1(R, d, \theta) = \sqrt{(R \cos \theta)^2 + (R \sin \theta - d)^2} = \sqrt{R^2 + d^2 - 2Rd \sin \theta} \quad (3)$$

Likewise, the angle θ_1 between the thruster centerline and the probe location can be expressed as :

$$\theta_1 = \begin{cases} \arctan(\tan \theta - \frac{d}{R \cos \theta}) & \text{for } \theta \in]-90^\circ; +90^\circ[\\ \theta & \text{for } \theta = \pm 90^\circ \end{cases} \quad (4)$$

These two equations can be generalized as:

$$r_{1,2} = \sqrt{R^2 + d^2 + 2kRd \sin \theta} \quad (5)$$

$$\theta_{1,2} = \begin{cases} \arctan(\tan \theta + k \frac{d}{R \cos \theta}) & \text{for } \theta \in]-90^\circ; +90^\circ[\\ \theta & \text{for } \theta = \pm 90^\circ \end{cases} \quad (6)$$

with $k = -1$ for A_1 and $k = +1$ for A_2 .

Thus, in the case of a thruster centerline not aligned with the probe at 0° position, the total ion current can be determined thanks to the following equation:

$$I_{i,tot} = \pi \int_{-\pi/2}^{\pi/2} r_{1,2}^2(\theta) j_i(\theta) \sin(\theta_{1,2}(\theta)) d\theta. \quad (7)$$

CLUSTER OPERATION

Geometric difficulties must be taken into account when considering Faraday cup measurements in the far-field plume of a cluster. As the probe focuses on two different point sources, it is impossible to assess from which source the ions collected come from. Moreover, the distance between anode blocks and the probe varies with the angle. To do so, correction factors must be rated to predict as precise as possible the total ion current of a cluster. For now, one correction factor has been found to take into account the variation of the distance between thruster exit planes and the probe location as a function of the angle:

$$\kappa_R = \left(1/2 \left(\frac{r_1(\theta)}{R} + \frac{r_2(\theta)}{R} \right) \right)^2 \quad (8)$$

FC measurements allow to determine various efficiencies related to the ion current density. Thus, the current utilization efficiency η_b describes the fraction of discharge current used to produce ion beam I_b (also named as $I_{i,tot}$):

$$\eta_b = \frac{I_{i,tot}}{I_d} \quad (9)$$

D. Retarding potential analyzer

A Retarding Potential Analyzer (RPA), also known as Retarding Field Electrostatic Analyzer (RFEA), is a gridded probe that uses electric fields acting as energy filters to selectively repel the constituents of a plasma or a beam.¹⁷⁻¹⁹ The RPA used in this experiment is built with four electrostatically-biased grids and a collector (conductor) placed behind the grids that serves as a charge detector. All grids as well as the collector are aligned inside a stainless steel housing. The electrostatic grid assembly used to analyze the ion flux includes the entrance or screen grid (G1), the electron repeller (G2), the ion filter (G3), and the second electron repeller (G4), of which the role is effectively described in the literature.^{18,20} An RPA acts as a high-pass filter: only ions with voltages that are energy-to-charge ratios, greater than the retarding grid voltage can pass and reach the collection electrode. The potential of the ion retarding grid is then varied while monitoring the ion current incident on the collector; thus, data are obtained as collector current versus discriminator voltage.

The grid voltage scheme was: G1 floating, G2 at -15 V, G3 swept from 0 to 400 V, G4 at -20 V and collector at -5 V. The overall shape of the I-V curve depends upon the RPA design and the grid voltages. Deviation from the true (unperturbed) I-V trace is usually due to secondary electron emission and ionization and charge-exchange collision events inside the RPA.¹⁹ The Semion control unit from *Impedans Ltd* has been used to power the RPA and acquire the I-V curves.

The negative derivative of the I-V trace is proportional to the ion velocity distribution function:¹⁹

$$\frac{dI}{dV} \propto -f(v) \text{ for } v \geq 0, \quad (10)$$

where I is the measured current, V the discriminator voltage, v is the ion velocity at the entrance of the RPA, and f the ion Velocity Distribution Function (VDF). The previous expression is only valid for $v \geq 0$ as ions moving away from the probe ($v < 0$) never reach its orifice. Note that, in the case of a grounded aperture grid, a measurement of the plasma potential at the RPA location is needed to retrieve the true ion VDF. The velocity of ions entering the RPA is not the velocity in the plasma but the velocity behind the sheath instead. Assuming a planar sheath and for a collisionless medium, the kinetic energy of the ion is

then increased by eV_p . In the course of this study, the entrance grid was floating and is supposed to be at the local plasma potential. However, an RPA does not measure the local ion VDF, whatever G1 voltage in fact, as all voltages have the ground as reference. Instead, it measures an accelerated VDF.¹⁷

The distribution function obtained from the first derivative of the current is called the Ion Energy Distribution Function (IEDF) when the velocity is converted into energy. However, the energy is then the energy of the ions along the direction of the RPA which is not necessarily the total kinetic energy. Only in the case of a perfectly collimated ion beam with a 0° divergence angle an RPA measures the total kinetic energy. As all electric propulsion devices have a non-zero divergence angle, ions might have a significant amount of kinetic energy in directions perpendicular to the thruster axis.

Characteristic dimensions of the 4-grids RPA operated during these experiments are given in Table 1.

The IEDF can provide two values: the mean ion energy E_{mean} computed from the first order moment of the IEDF (see Equation 11) and the most probable energy E_{max} that corresponds to the energy of the highest peak.

$$E_{mean} = \frac{\int_0^{V_{max}} \frac{\partial I}{\partial V} \times V dV}{\int_0^{V_{max}} \frac{\partial I}{\partial V} dV} \quad (11)$$

With V_{max} the upper limit value of the filtering bias voltage.

Table 1: RPA—Characteristic dimensions.

Characteristic dimensions	
Mesh size (mm)	0.4
Diameter (mm)	45
Length (mm)	40
Transparency (%)	60.2
Distance between grids (mm)	2
Collimator diameter (mm)	10

III. Results and discussion

A. Far-field plume properties for single thruster

The following section introduces plume characterization of a single thruster operation. Plasma plume properties measurements of a single thruster head were performed in configurations X1 and X2. In the case of the X2 configuration, each anode block was investigated independently. Such measurements are useful not only for plume comparison between single thruster and cluster operations, but also to verify how thruster position regarding the probe alignment influences plume properties.

1. Ion current density angular profiles and total ion current

The overall shape of the ion current density angular profile remains similar in many features whatever the operating conditions, as shown in the set of Figures plotted below. Indeed, the distribution is axisymmetric with respect to the thruster centerline $\theta = 0^\circ$ and reaches a maximum amplitude at this point. When moving away from the thruster centerline, the ion current density sharply decreases by an order of magnitude.

While HTs' design remains the same, (i.e. magnetic field topology, discharge channel (material and size)), they are however experimental models. They are more subject to small differences, which could impact operation and performances. To do so, the repeatability of FC measurements have been investigated to verify the plume similarity between different anode blocks. For same operating conditions, the ion current density angular profiles were recorded for both ISCT100v2-ICARE-01 and -03, as seen in Figure 6.

Regarding the two angular profiles obtained for two different thrusters, one would observe that while the

shape is conserved, some quantitative differences are observable, especially at larger angles. Notwithstanding, the total ion current computed for two thrusters remains roughly the same, within a decent margin of error around 4 %, namely 0.382 A and 0.367 A for ISCT100v2-ICARE-01 and -03, respectively.

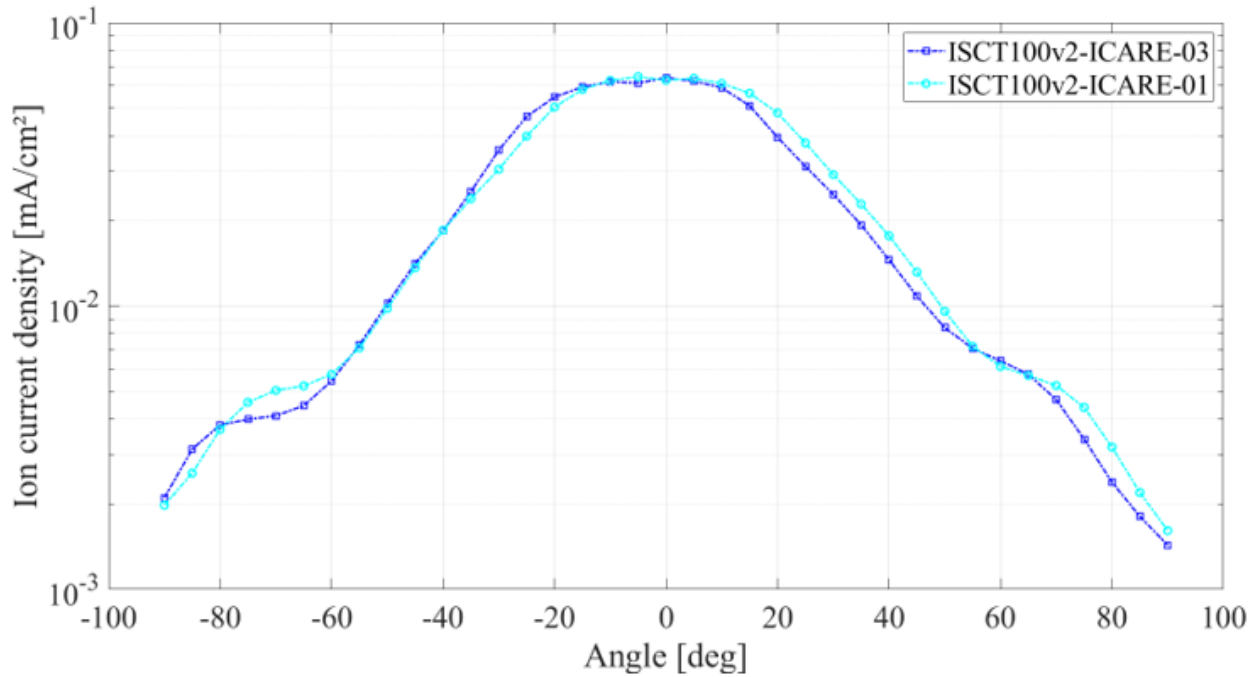


Figure 6: Ion current density angular profiles for ISCT100v2-ICARE01 and -03, at same operating conditions 300 V and 6 sccm

Figure 7 shows the j_i angular distribution for two different anode mass flow rates, i.e. 5 sccm and 6 sccm, at 300 V anode voltage. The shape of the two profiles remains the same, while the total ion current increases with the anode mass flow, as expected. Since the neutral density increases in the discharge channel of the HT, ionization collisions become more likely, favoring ions production.

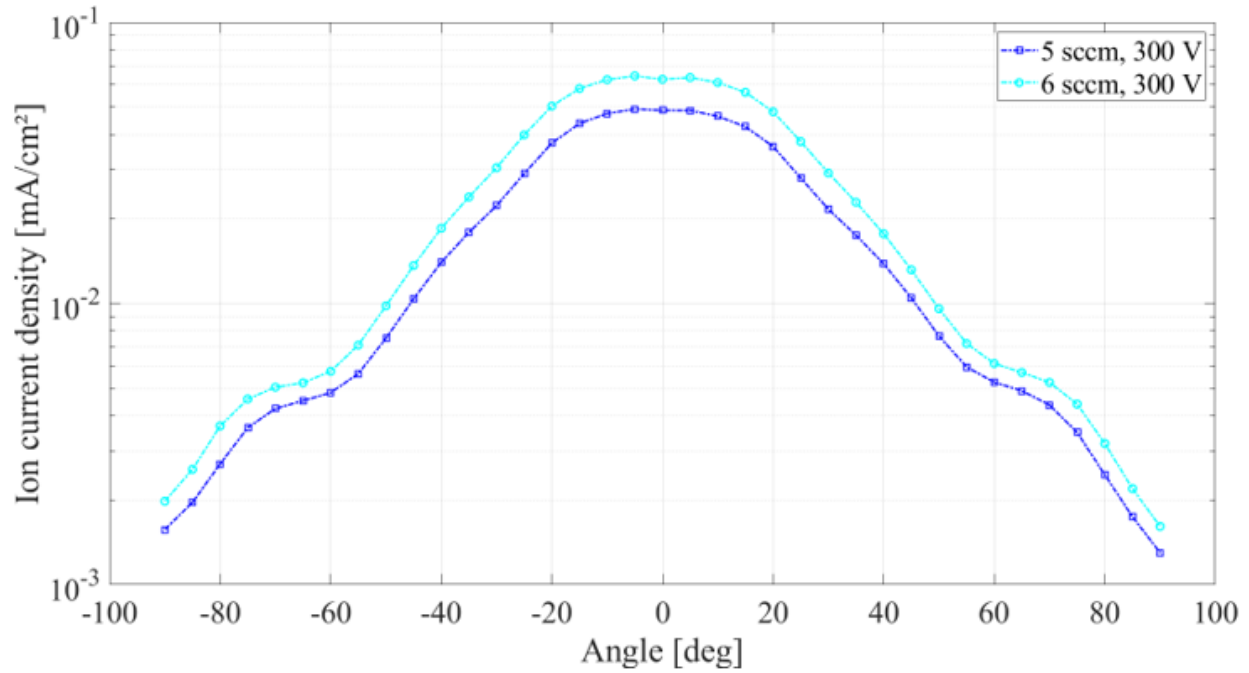


Figure 7: Ion density angular profiles for the thruster operated at 300 V and two different anode mass flow rates, namely 5 sccm and 6 sccm.

The influence of the anode voltage has been investigated for 6 sccm injected in the anode for the thruster operated at 200 V and 300V. The respective j_i angular distributions are plotted in Figure 8. Specific features are identifiable. Firstly, the current density increases in the core of the plume as U_d is amplified. Secondly, the ion current density increases at large angles when the discharge voltage is ramped up. Thirdly, at high voltage condition, a hump is observed around $\pm 60^\circ$, while it is less pronounced for the 200 V condition. Such observation is directly linked to the plume divergence. As the discharge voltage is ramped up, the beam is more focused, i.e. most of the ion flux is concentrated in the core of the plume.

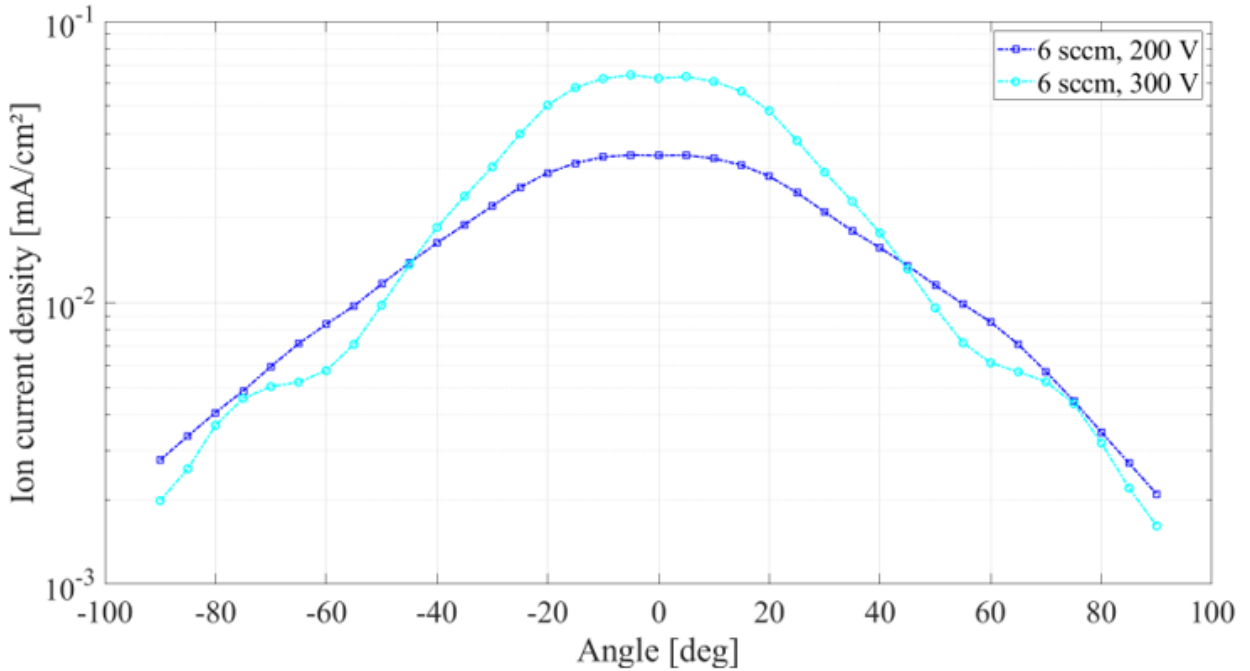


Figure 8: Ion density angular profiles for the thruster operated at 6 sccm and two different anode voltages, namely 200 V and 300 V.

The total ion current has been computed for the different configurations at 300 V, 6 sccm. The beam efficiencies can also be determined to have consistent comparisons as operating conditions (namely the discharge current) can vary between different anode blocks and configurations. The set of data are visible in Table 2 for configuration X1 and X2. One could observe that for single operation the configuration does not impact the performances of the THDs as the beam efficiency is sensitively the same for each THD in a given configuration, in the range of 0.8 – 0.9. Similar tendencies were reported in other far-field plume characterization.^{21, 22}

Table 2: . Total ion current for monolithic HT operation in different configurations.

Configurations	\dot{m}_a [sscm]	U_d [V]	$I_{i,tot}$ [A]
Single	6	300	0.382
THD1 (X2)	6	300	0.418
THD2 (X2)	6	300	0.37

2. Ion energy spectra

The ion energy distribution function is investigated. Figure 9 shows the different IEDF obtained for a single THD operated at 300 V, 6 sccm in configuration X1. Each IEDF is normalized to its maximum amplitude for a sake of clarity. On the centerline of the thruster ($\theta = 0^\circ$), a primary peak is visible at 250 eV that means 83% of the discharge voltage. The difference between these two values is in part the consequence of the CRP that is the energy required to extract electrons from the cathode. As previously mentioned, the CRP was maintained to -10 V in the course of this study, by adjusting the heating power. Other main loss terms are ionization, plasma-wall interactions, beam divergence, and overlap between the ionization and acceleration regions. This primary peak can be identified as source ion population created by collisions between the magnetized electrons and the injected gas particle. As we move away from the centerline, a large population of intermediate energy ions is also visible, of which the fraction increases with the angle.

This ion population might be the result of different mechanisms. Firstly, source ions undergo elastic collision resulting in the loss of momentum. Secondly, some ions are accelerated in regions of low plasma potentials where magnetic field lines have greater curvatures. These mechanisms result in low energetic ions, collected in the off-centerline region.

Same observations can be extended to single thrusters operated in Configurations X2 as seen in Figure 10. Notwithstanding, one can observe that the ion flux reaching the RPA collector varies significantly with the probe position, i.e. with the position of one thruster head relative to the probe. Indeed, for THD1, ion flux collected is quite different between -20° and 20° positions. As the probe is closer to the THD1 in positive angle, the ion flux is also higher.

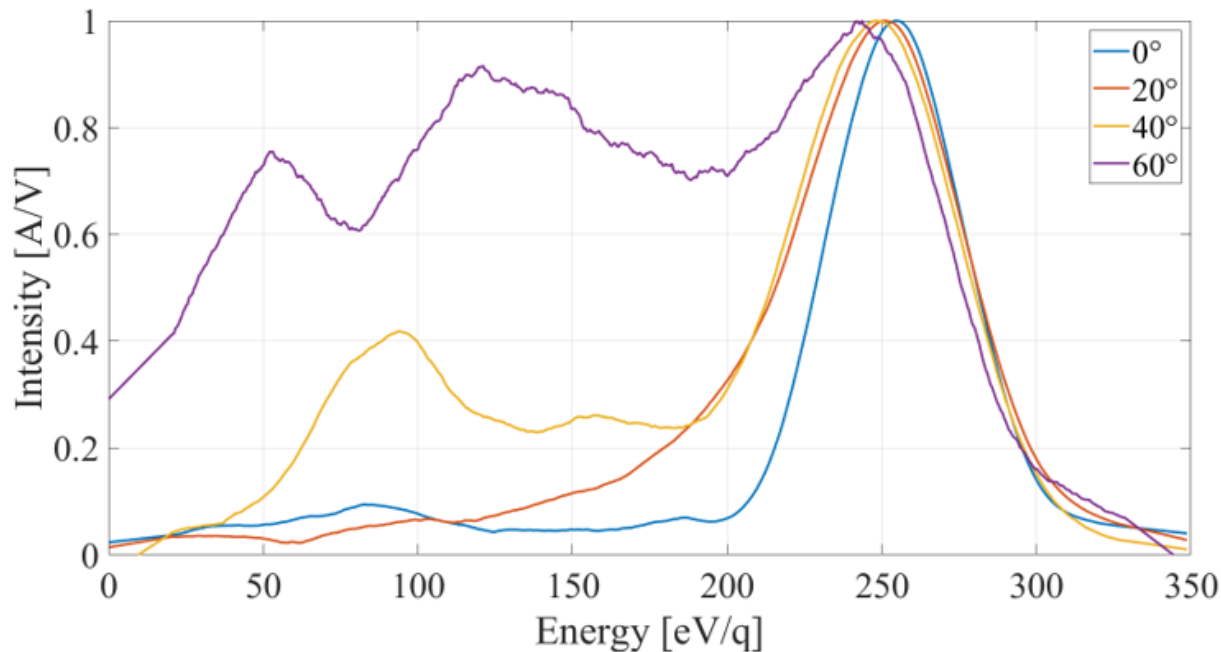


Figure 9: IEDF for a single THD operated at 300 V, 6 sccm in configuration X1.

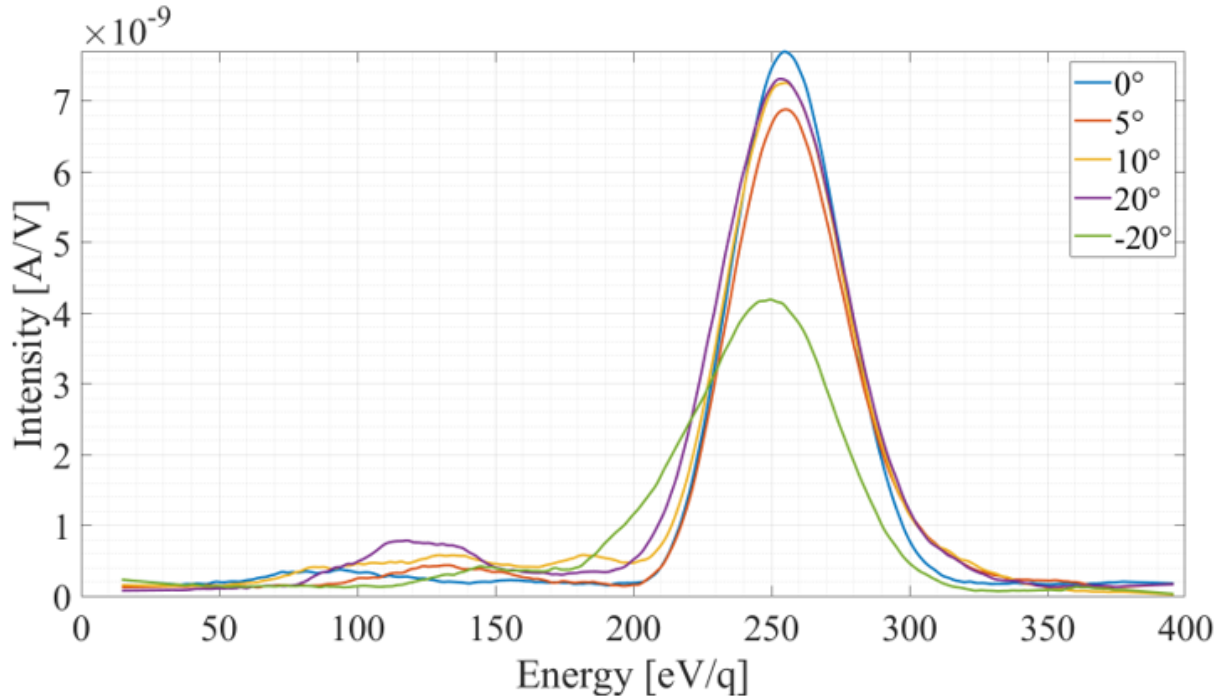


Figure 10: . IEDF for THD1 operated at 300 V, 6 sccm in configuration X2.

The evolution of both the most probable (E_{max}) and mean energy (E_{mean}) are plotted in Figure 11 as function of the angle for one single thruster head operated at 300 V and 6 sccm, in configuration X1. Regarding the E_{max} distribution along the angular profile, the drop at $\pm 60^\circ$ is clearly identified. It confirms the trend observed in the previous section. Furthermore, below this drop, the E_{max} distribution is maximum around 0° and remains quite constant towards larger angles. This section of the plume is then dominated by high-energy ions, of which the energy is closed to the discharge voltage. Hereafter the drop, E_{max} decreases, pointing out that this region is dominated by slow-moving ions, resulting from CEX collisions. Nevertheless, the E_{mean} distribution presents different structure. The mean energy is maximum at the thruster centerline, since the ion beam is dominated by source ions and less disturbed by collision events with background pressure. When moving towards large angles, the mean energy distribution steadily decreases, as the low-energy ion population increases with angles to become predominant. Such observations are similar to what was describe in previous campaigns.²¹ Same observation can be made for X2 configuration considering that the distribution is shifted toward positive or negative angle, as the RPA is not directly aligned with the thruster centerline at the 0 degree position (see Figure 12). Notwithstanding, both the amplitude and the shape of the distributions are sensitively conserved.

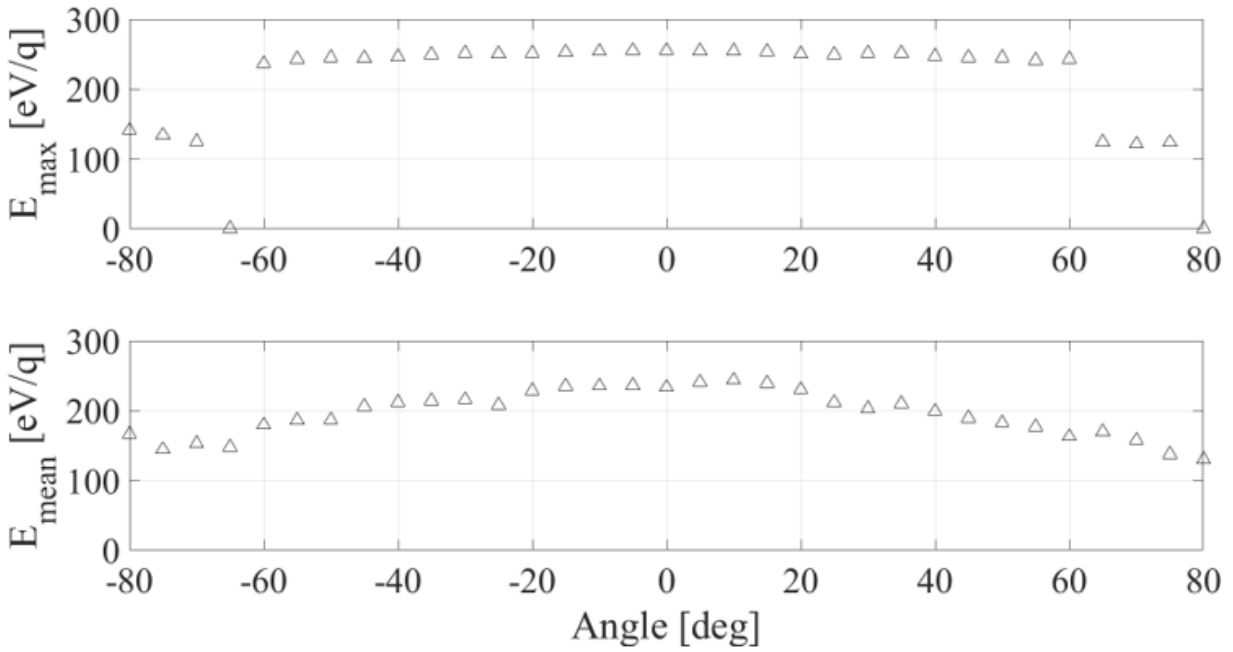


Figure 11: Angular profiles of the most probable energy (E_{max}) and the mean energy (E_{mean}) for one single THD operated at 300 V, 6 sccm in configuration X1.

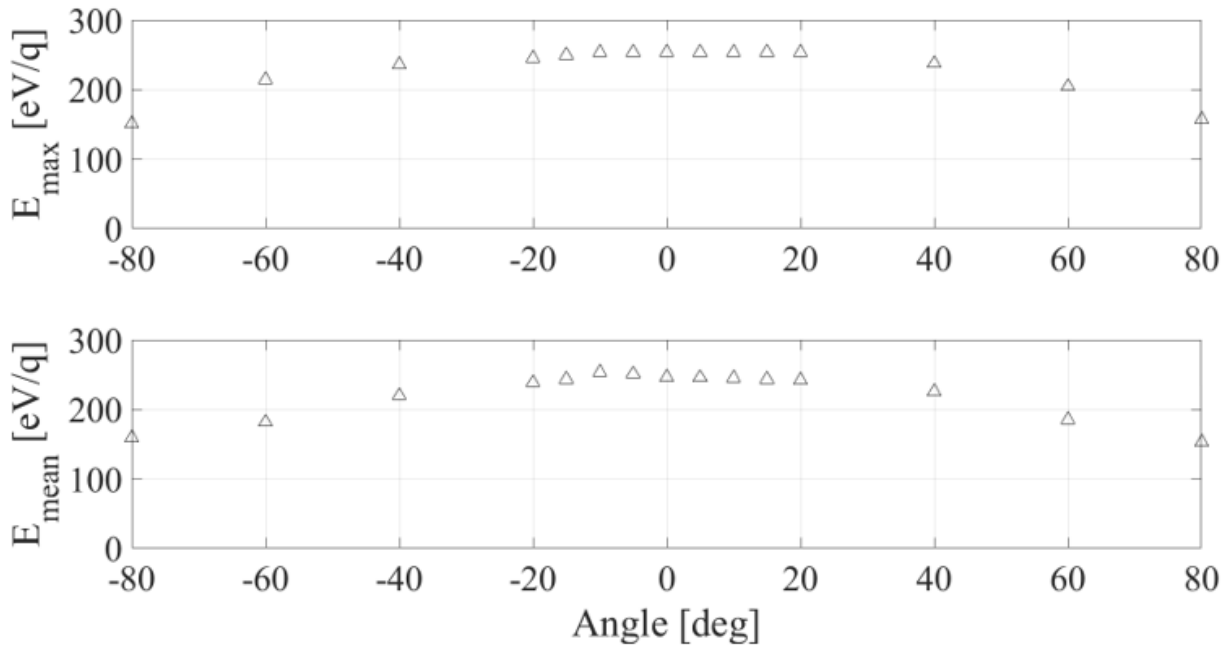


Figure 12: Angular profiles of the most probable energy (E_{max}) and the mean energy (E_{mean}) for THD1 operated at 300 V, 6 sccm in configuration X2.A.

B. Far-field plume properties for cluster configuration X2

1. Ion current density angular profiles and total ion current

Ion current density profiles measured for cluster operations are presented in this section. The angular profiles are compared to single thruster operation. Thus, THD1 and THD2 profiles are the one measured for

single thruster operations. Cluster profile is the one obtained for cluster operation, while THD1 + THD2 is obtained by summing profiles of single thruster operations. The ratio between the ion current density of cluster and the sum of the two thruster heads is also plotted for different angles.

Figure 13 represents the angular profiles for thruster operated at the same operating parameters, namely 300 V and 6 sccm. The shape of the ion current density profile for cluster operation is similar to a single thruster operation. Indeed, the distribution is axisymmetric with respect to the cluster centerline $\theta = 0^\circ$ and reaches a maximum amplitude at this point. When moving away from the cluster centerline, the ion current density sharply decreases by an order of magnitude. Around $\pm 60^\circ$, the wing structure is visible and well traced for the 300 V conditions.

When summing the ion flux of the two single thrusters, same shape is observable. Notwithstanding, the ion current density near the cluster centerline tends to be underestimated as the ratio is higher than 1. On the other hand, when moving away from the core of the plume, the trend is reversing as the prediction fell short of 1. Same tendencies have been observed in the plume of a cluster of two BHT-200.²³ This trend is believed to be related to plasma potential distribution in the plume of a cluster. Also, as local background pressure increases in the vicinity of the cluster exit plane, CEX ions production are favored and directed toward large angles.

Figure 14 shows the angular profile for thruster operated at different discharge voltages. The shape of the ion current density profile clearly appears to be a combination of angular profiles of 200 V and 300 V operations. While the distribution is axisymmetric with respect to the cluster centerline and reaches a maximum amplitude at this point, the wing structure diverges according to the operating parameters. Indeed, on the side on which thruster is operated at 300 V (negative angle), the wing shape is clearly visible around $\pm 60^\circ$ and typical of high voltage operations.

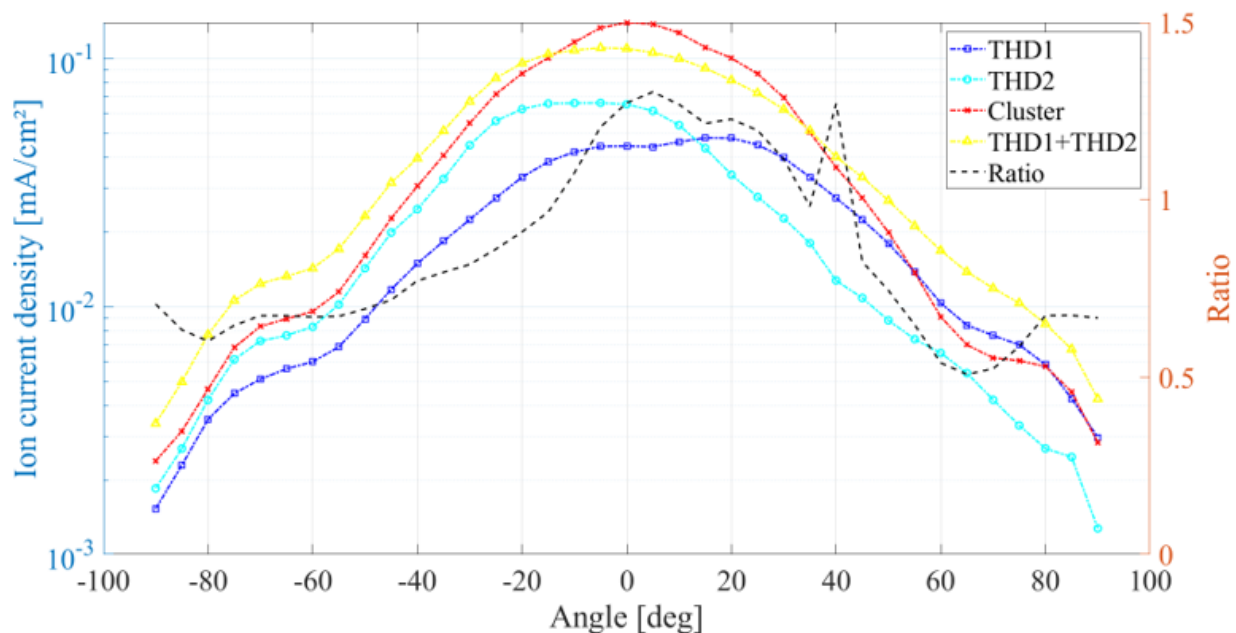


Figure 13: Ion current density profiles for thrusters operating at 300 V, 6 sccm in Configuration X2.A.

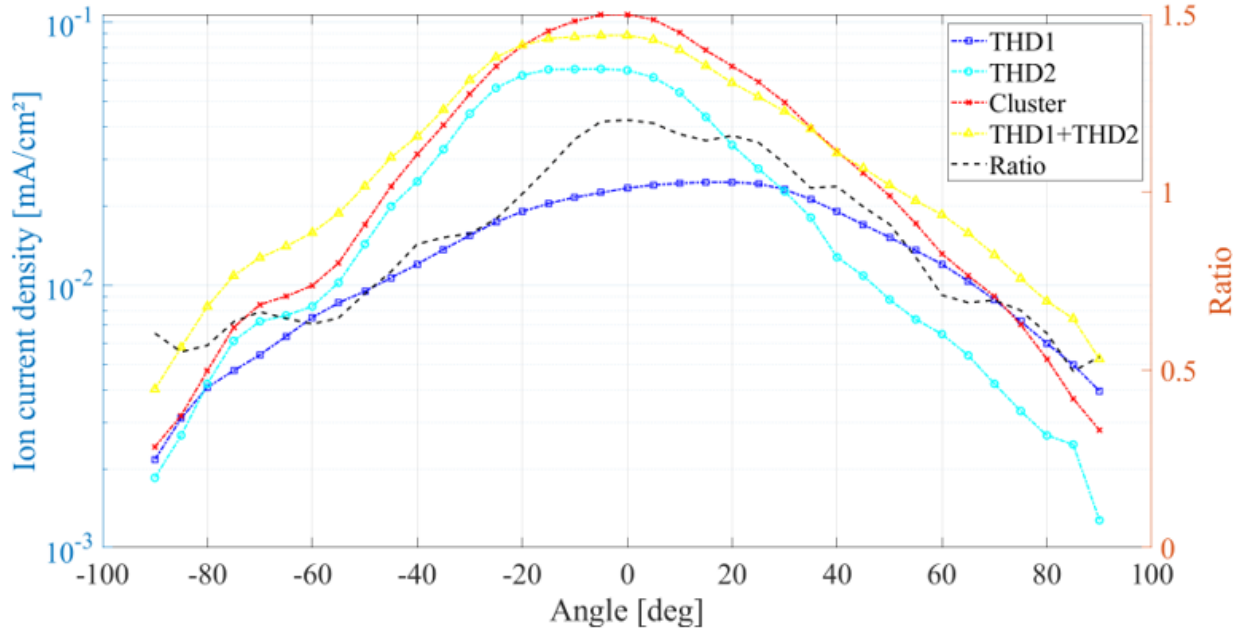


Figure 14: Ion current density profiles for thrusters operating at $U_{d1} = 200$ V and $U_{d2} = 300$ V, 6 sccm in Configuration X2.A.

The total ion current can be determined from the ion current density angular profiles presented above, using the equations introduced in Section C. Table 3 list the total ion current computed for different discharge parameters, in the cases of cluster and monolithic configurations. A bar chart is plotted in Figure 15 to compare beam efficiencies of cluster and the sum of single thruster at 300 V. A comparison between each cluster configuration is also proposed.

One can observe that beam efficiency is depreciated for cluster plume measurements compared to the sum of two single thrusters. While the model to calculate the total ion current in the cluster plume can be challenged for now, such efficiency differences can however be explained by inherent properties due to cluster operation. Indeed, it has been shown in the plume of the cluster of BHT-200,²³ that the electric field is reversed in the region of the cluster centerline. This causes slow moving ions to be accelerated towards the cluster radiator. Also, the interactions between the two plumes can favor elastic and CEX collisions. As a result, ions are deflected toward large angles as observed in the different angular profiles. In other terms, the beam divergence increases.

While the beam efficiency is the same for single thruster operation whatever the configuration, performance differences are observable in the case of cluster operation. Indeed, the beam efficiency is about 76% and 68% for Configuration X2.A and X2.B, respectively. Such drop can be associated to magnetic field interactions due to the proximity of the two anode blocks in configuration X2.B. Indeed, this will impact both the electron confinement and the electric field distribution in this region. While magnetic field lens could not be mapped for Configuration X2.A due to the space limitation of the magnetic characterization bench, one can assume that such tendency is less pronounced for this configuration as the magnetic field strength decreases with the cube of the distance.

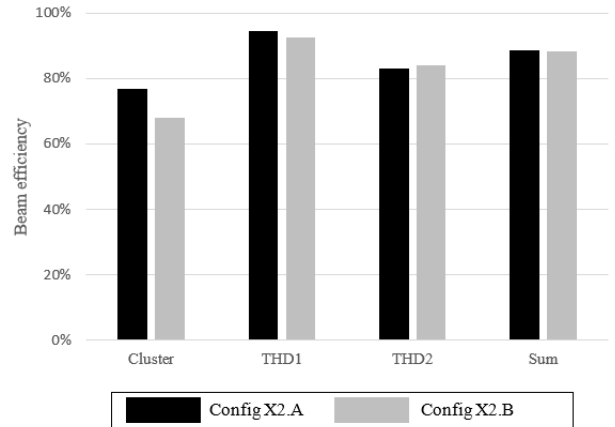


Figure 15: Beam efficiency comparison between cluster and sum of single thruster head operations at $\dot{m}_a = 6$ sccm and $U_{d1} = 300$ V and $U_{d2} = 300$ V.

Table 3: . Total ion current for X2 cluster operation.

THD1		THD2		Cluster	THD1	THD2	Sum
\dot{m}_a [sccm]	U_d [V]	\dot{m}_a [sccm]	U_d [V]				
6	300	6	300	0.71	0.42	0.39	0.81
6	200	6	200	0.6	0.32	0.35	0.67
6	300	6	200	0.66	0.42	0.35	0.77
6	200	6	300	0.64	0.32	0.39	0.71

2. Ion Energy

The ion energy distribution function is investigated. Figure 16 shows the different IEDF obtained for cluster operated at 300 V, 6 sccm in configuration X2.A. On the centerline of the thruster $\theta = 0^\circ$, a primary peak is visible at 255 eV, in agreement with what was observed for single thruster operation. As we move away from the centerline, a large population of intermediate energy ions is also visible, of which the fraction increases with the angle. In the same time, source ion fraction decreases with the angle. Thus, for a given discharge voltage condition, both cluster and single thruster operation are comparable in terms of content.

A direct comparison is also proposed between IEDF measured for single thruster in configuration X1 and cluster in configuration X2.A at 0 degree position, at 300 V and 6 sccm (see Figure 41). While the shape is conserved, i.e. a large peak is observable at 255 eV, the profiles differ in amplitude and broadening. Indeed, ion flux intensity is higher for cluster operation as RPA collects ion from the plumes. Also, the broadening can be estimated thanks to the full width at half maximum (FWHM). Thus, the FWHMs are about 70 eV/q and 60 eV/q, for cluster and single thruster operation respectively. The increase of the broadening is caused by elastic collisions between beam ions and background chamber gas particles, that are favoured for cluster operation.

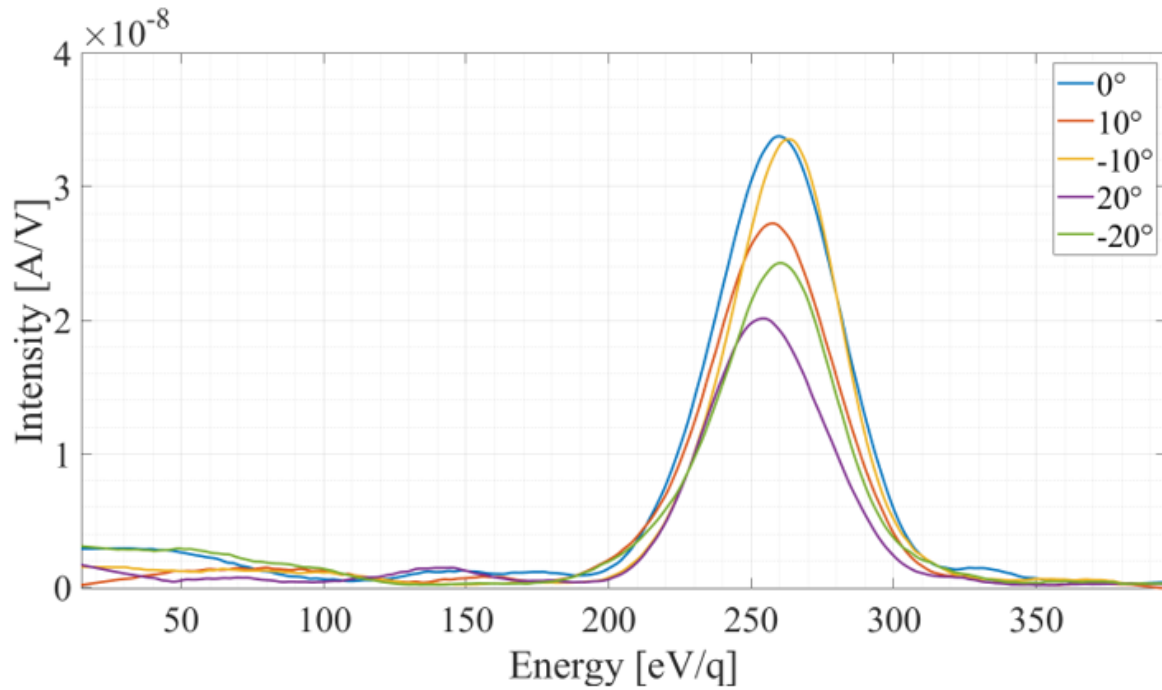


Figure 16: IEDFs for cluster operated at 300 V, 6 sccm at different angular positions

The ion energy distribution function is also investigated for thrusters operated at different voltages, namely $U_{d1} = 200V$ (positive angle) and $U_{d2} = 200V$ (negative angles) at 6 sccm. On the cluster centerline, the 300 eV/q ions population is in higher quantity than the 200 eV/q ions. This is consistent with the fact that ion production is favored when the discharge voltage is ramped up. As the probe is moved toward positive (negative) angles, the 200 eV/q (300 eV/q) ion population increase relative to 300 eV/q ions (200 eV/q), until becoming predominant at 20°. Indeed, the RPA is in the far-field plume of anode block operated at 200 V (300 V). The probe will preferentially collect ions from this anode block, as the other ion population is partially screened by its plume.

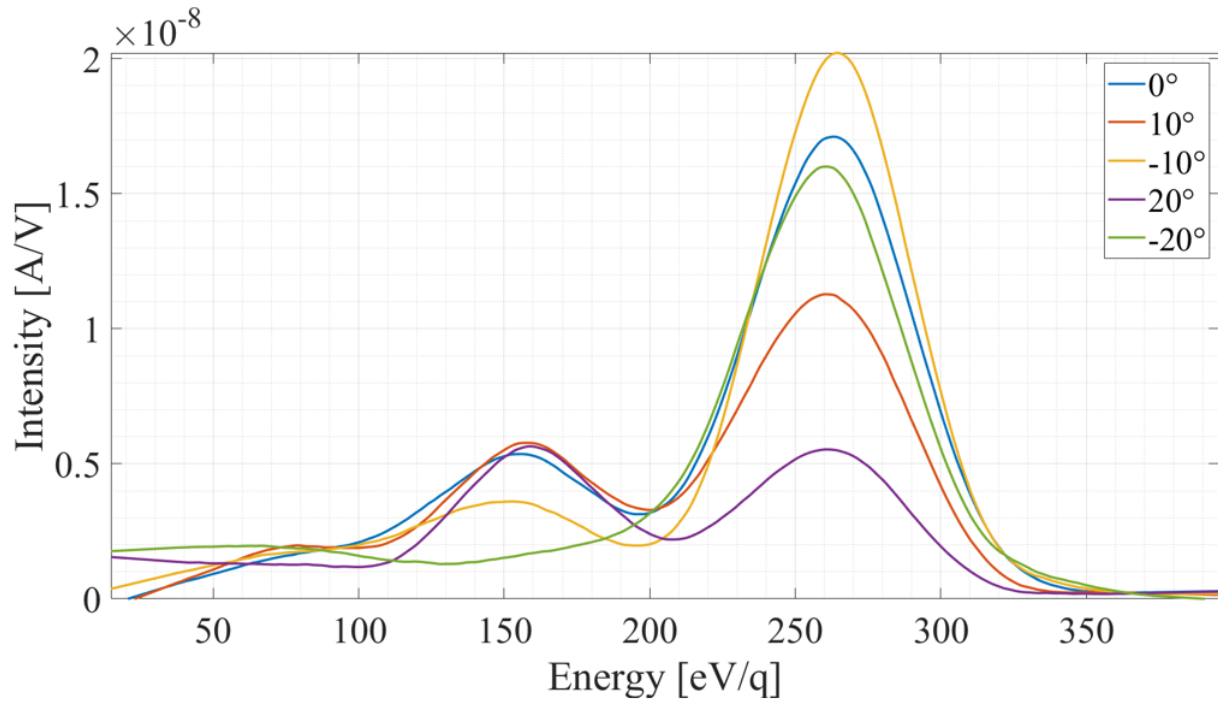


Figure 17: IEDFs for cluster operated at $U_{d1} = 200$ V and $U_{d2} = 300$ V and 6 sccm.

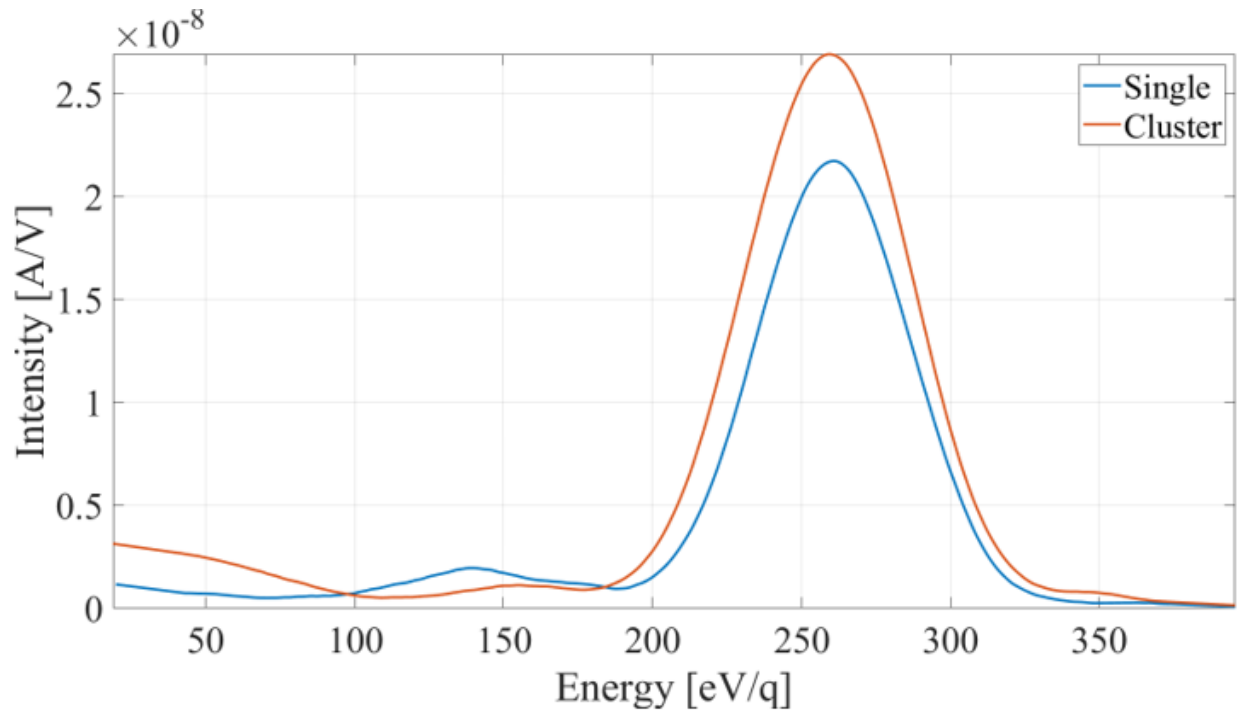


Figure 18: . IEDF comparison between single thruster (configuration X1) and cluster operation (configuration X2.A) at 300 V and 6 sccm for $\theta = 0^\circ$.

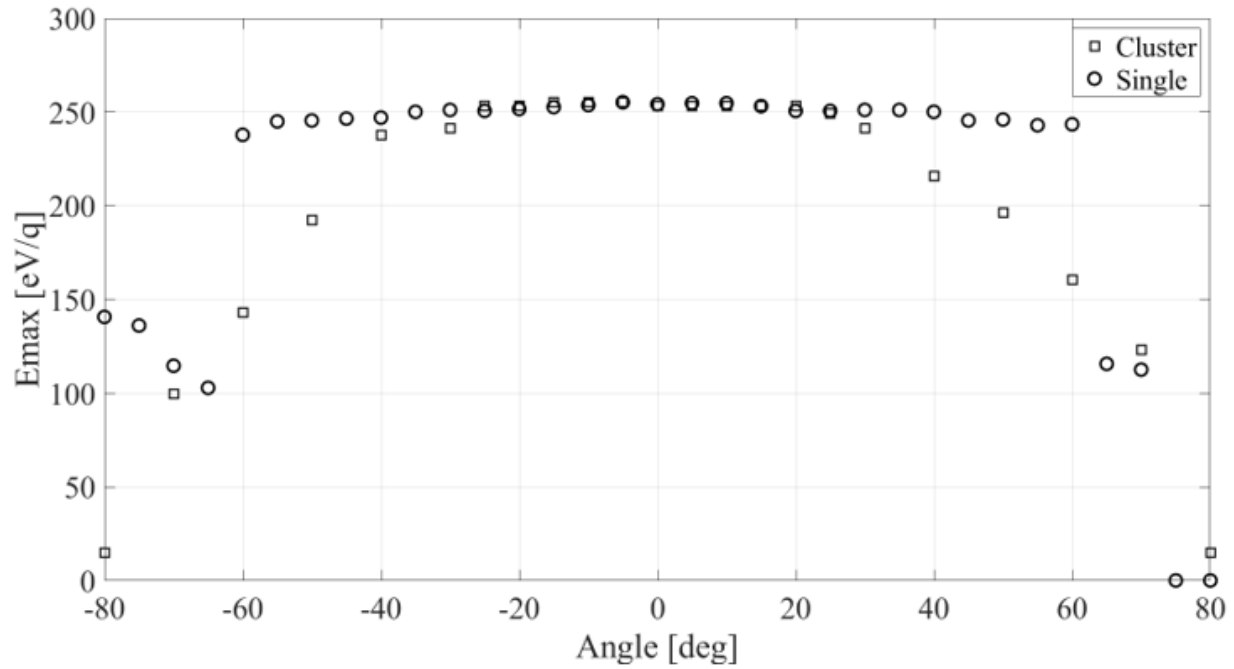


Figure 19: E_{max} for cluster (X2.A) and single thruster operations at 300 V and 6 sccm.

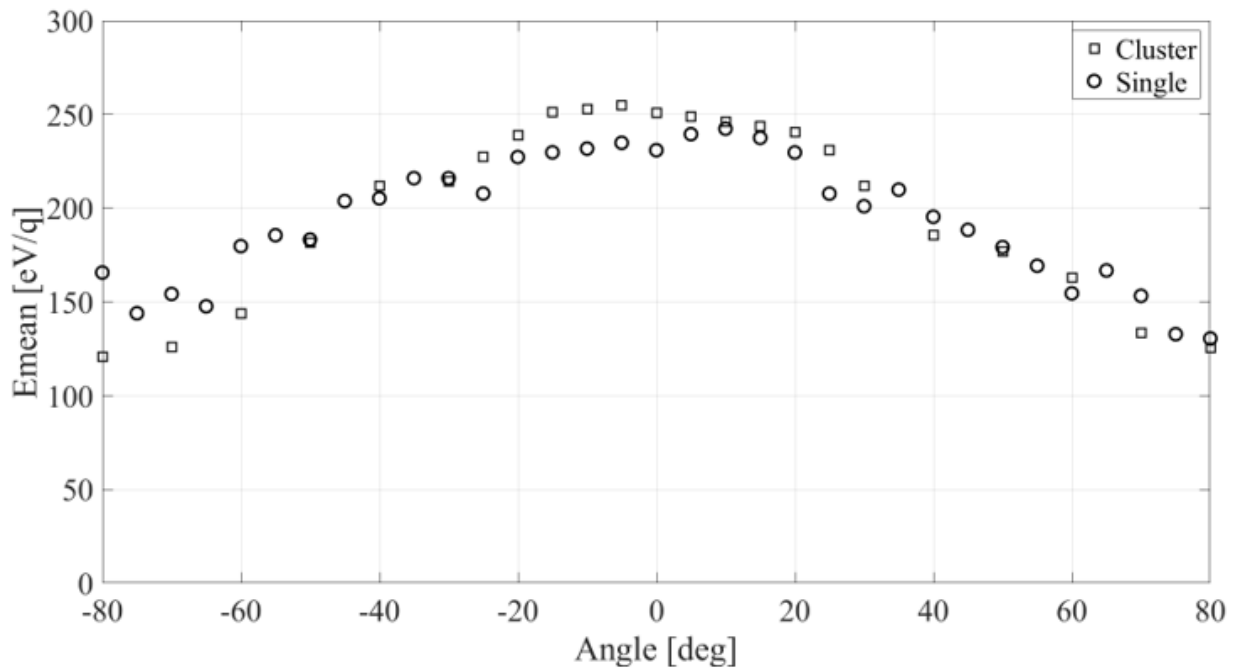


Figure 20: E_{mean} for cluster and single thruster operations at 300 V and 6 sccm.

The mean and most probable energies are determined for cluster operated at 300 V and compared with single thruster operation, as shown in Figures 19 and 20. The E_{max} angular distribution depicts same tendencies for both cluster and single thruster operation. The energy is maximum in the core of the plume at a same amplitude level and decreases at large angles. Nevertheless, the break usually observed around $\pm 60^\circ$ for single thruster operation appears around $\pm 40^\circ$ for cluster operation. Thus, one can say that

cluster operation does not affect the magnitude of the most probable energy in the core of the plume. The E_{mean} angular distribution also displays same shape for both mode operations, while the magnitude are quite different. Indeed, in the core of the plumes, E_{mean} appears to be lower for cluster operation and reaches comparable amplitudes as the one of single thruster operation at larger angles. Such differences observed in the core of the plume can be explained by the interaction between the two plumes that favours collisions and thus creation of low-energy ions, as explained in the previous section. Also, as the background pressure increases in the vicinity of the two thrusters, CEX collisions are more likely.

C. Far-field plume properties for cluster configuration X2-SC

In this X2-SC configuration, the cathode is the electrical common point and is the only source of electrons for the two anode blocks. all electrical parameters decrease when the cathode is moving from closest to the furthest position. Regardless the cathode moving direction, discharge current, CRP and KRP tendencies are similar in function of the cathode position. Moreover, we can see less than 60mA of differences between the two anode blocks. That could be due either to different anode mass flow injected in the discharge channel (internal gas leakgas leak along the anode line) or to different distances cathode – Anode anode 1 and cathode – anode 2 ($< 1\text{mm}$), that could imply a preferential electronic path towards one anode block due to the magnetic topology close to the cathode.

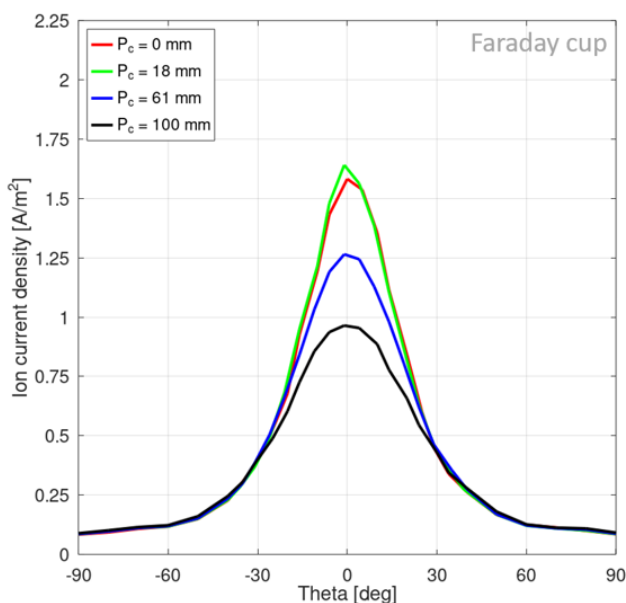


Figure 21: Ion current density profile as a function of the cathode position.

The diminution of the discharge current with the increasing cathode position, indicates less electrons collected by the anode and going through the magnetic barrier. This is associated to an increasing voltage of the CRP and KRP (in absolute value), which could indicate higher sputtering energy needed to maintain a high emitter temperature when the cathode is moving far away from the cluster. This increasing distance could imply either electrons emitted by the cathode and collected by others metallic surfaces than the anode (due to the increasing path cathode-anode) or to the reduction of the magnetic field intensity which (in the closest position) could help electrons to move from the cathode to the anode.

We can also observe a decreasing extracted ionic current (for the FC) associated to an increasing divergence at 90%. The following figure show us the effect of the cathode position on the extracted current measured by the Faraday cup

IV. Conclusion

The far-field plume properties in terms of ion current density and ion energy has been characterized for different cluster configurations, namely a cluster of two thrusters and a cluster of two thrusters using a shared cathode moving from a close to a far position. Ion current density angular profiles were measured thanks to a Faraday cup in the far field plume of single thruster and cluster. While the shape of the two operation modes remains identic, differences are observed in terms of magnitude. Indeed, the ion current density angular profiles measured in the plume of a cluster tends to be higher in the core of the plume and lower at larger angles compared to the sum of ion current density angular profiles of two single thrusters. Furthermore, efficiency analysis has revealed interesting features. The beam efficiency appeared to be lower for cluster operation. Also the configuration X2.B exhibits lower performances than configuration X2.A, associated to magnetic field interactions.

Ion energy has been investigated thanks to a 4-grid RPA. The shape of the IEDFs measured in the plume of a cluster is comparable to the one observed for a single thruster operation. Notwithstanding, the broadening of the main peak appears to be higher for cluster operation, as the interactions between the two plumes favours elastic collisions. Also, E_{mean} and E_{max} angular distribution analysis have shown that while the most probable energy remains unchanged in both mode operations, the overall energy of ions remains lower for cluster operation.

Also, the cathode position clearly affects the cluster parameters by reducing the extracted ionic current and increasing the divergence at 90% (associated to an increasing of CEX) when the cathode-cluster axis distance increases.

In future works, cluster of two thrusters must be characterized in terms of thrust measurements and compared with single thruster operation. Alternative cluster configurations will be also investigated, namely a cluster of three 100 W-class Hall thrusters. Such works are interesting for systems integrations and to gain insight on how cluster operations influence plume content and performances. Finally, LIF spectroscopy and $E \times B$ probe measurements will be performed to understand how plumes interact between each other.

References

- ¹S. Mazouffre, “Electric propulsion for satellites and spacecraft : established technologies and novel approaches,” *Plasma Sources Science and Technology*, vol. 25, pp. 1–27, 2016.
- ²B. E. Beal, A. D. Gallimore, and W. A. Hargus, “The effects of clustering multiple Hall thrusters on plasma plume properties,” in *39th AIAA/ASME/SAE/ASEE Joint Propulsion Conference and Exhibit, Huntsville, Alabama, The United States of America, July 20-23*, no. 2003-5155, pp. 1–10, 2003.
- ³M. L. R. Walker and A. D. Gallimore, “Hall thruster cluster operation with a shared cathode,” *Journal of Propulsion and Power*, vol. 23, no. 3, pp. 528–536, 2007.
- ⁴B. E. Beal, *Clustering of Hall Effect Thrusters for High-Power Electric Propulsion Applications*. PhD thesis, Univeristy of Michigan, 2004.
- ⁵O. Duchemin, A. Lorand, M. Notarianni, D. Valentian, and E. Chesta, “Multi-Channel Hall-Effect Thrusters: Mission Applications and Architecture Trade-Offs,” *30th International Electric Propulsion Conference, Florence, Italy, September 17-20*, no. 2007-227, pp. 1–15, 2007.
- ⁶O. Duchemin and D. Valentian, “Thrust vector control using multi-channel hall-effect thrusters,” in *43rd AIAA/ASME/SAE/ASEE Joint Propulsion Conference and Exhibit, Cincinnati, Ohio, The United States of America, July 8-11*, vol. 2, pp. 1–10, 2007.
- ⁷S. O. Tverdokhlebov, A. V. Semenkin, V. I. Baranov, L. E. Zakharenkov, and A. E. Solodukhin, “Consideration of cluster design approach for high power Hall propulsion,” in *41st Aerospace Sciences Meeting and Exhibit, Reno, Nevada, The United States of America, January 6-9*, no. 2003-494, pp. 1–5, 2003.
- ⁸J. Biron, N. Cornu, H. Illand, M. Serrau, R. Rigollet, and H. L. Gray, “The Thruster Module Assembly (Hall Effect Thruster) design, qualification and flight,” in *29th International Electric Propulsion Conference, Princeton, New Jersey, The United States of America, October 31 - November 4*, no. 2005-213, pp. 1–7, 2005.
- ⁹O. Duchemin, H. Illand, M. Saverdi, U. Cesari, M. Signori, D. Pagnon, and D. Estublier, “Testing of a thrust steering device on the PPS@1350 Hall thruster,” *42nd AIAA/ASME/SAE/ASEE Joint Propulsion Conference Exhibit, Sacramento, California, The United States of America, July 9th-12th*, no. 2006-4478, pp. 1–22, 2006.
- ¹⁰J. J. Szabo, R. Tedrake, E. Metivier, S. Paintal, and Z. Taillefer, “Characterization of a One Hundred Watt, Long Lifetime Hall Effect Thruster for Small Spacecraft,” in *53rd AIAA/SAE/ASEE Joint Propulsion Conference and Exhibit, Atlanta, Georgia, The United States of America, July 10-12*, no. 2017-4728, 2017.
- ¹¹S. Mazouffre and L. Grimaud, “Characteristics and Performances of a 100-W Hall Thruster for Microspacecraft,” *IEEE Transactions on Plasma Science*, vol. 46, no. 2, pp. 330–337, 2018.
- ¹²Y. Azziz, M. Martinez-Sanchez, and J. J. Szabo, “Effect of Discharge Voltage on Plume Divergence of a High Specific Impulse Hall Thruster,” in *41st AIAA/ASME/SAE/ASEE Joint Propulsion Conference and Exhibit, Tucson, Arizona, The United States of America, July 10-13*, no. 2005-4403, pp. 1–14, 2005.
- ¹³S. Mazouffre, G. Largeau, L. Garrigues, C. Boniface, and K. Dannenmayer, “Evaluation of various probe designs for measuring the ion current density in a Hall thruster plume,” in *35th International Electric Propulsion Conference, Atlanta, Georgia, The United States of America, October 8-12*, no. 2017-336, pp. 1–17, 2017.
- ¹⁴V. Hugonnaud and S. Mazouffre, “Optimization of a Faraday Cup Collimator for Electric Propulsion Device Beam Study : Case of a Hall Thruster,” *Applied Science*, vol. 11, no. 2419, pp. 1–29, 2021.
- ¹⁵G. Gerdin, W. Stygar, and F. Venneri, “Faraday cup analysis of ion beams produced by a dense plasma focus,” *Journal of Applied Physics*, vol. 52, no. 5, pp. 3269–3275, 1981.
- ¹⁶J. Vaudolon, *Electric field determination and magnetic topology optimization in Hall thrusters*. PhD thesis, Université d’Orléans, 2015.
- ¹⁷N. Gulbrandsen, Fredriksen, J. Carr, and E. Scime, “A comparison of ion beam measurements by retarding field energy analyzer and laser induced fluorescence in helicon plasma devices,” *Physics of Plasmas*, vol. 22, no. 3, pp. 1–15, 2015.
- ¹⁸D. Gahan, B. Dolinaj, and M. B. Hopkins, “Comparison of plasma parameters determined with a Langmuir probe and with a retarding field energy analyzer,” *Plasma Sources Science and Technology*, vol. 17, no. 3, 2008.
- ¹⁹C. Böhm and J. Perrin, “Retarding-field analyzer for measurements of ion energy distributions and secondary electron emission coefficients in low-pressure radio frequency discharges,” *Review of Scientific Instruments*, vol. 64, no. 1, pp. 31–44, 1993.
- ²⁰T. Hallouin, S. Mazouffre, M. Inchingolo, A. Gurciullo, P. Lascombes, and J.-L. Maria, “Far-field plume diagnostic of the 100 W-class ISCT100-v2 Hall thruster,” in *36th International Electric Propulsion Conference, University of Vienna, Austria, September 15-20*, no. 2019-617, pp. 1–32, 2019.
- ²¹T. Hallouin and S. Mazouffre, “Far-field plume characterization of a 100-W class Hall thruster,” *Aerospace*, vol. 58, no. 7, pp. 1–21, 2020.
- ²²R. R. Hofer and A. D. Gallimore, “High-Specific Impulse Hall Thrusters , Part 2 : Efficiency Analysis,” *Journal of Propulsion and Power*, vol. 22, no. 4, pp. 732–740, 2006.
- ²³B. E. Beal, A. D. Gallimore, J. M. Haas, and W. A. Hargus, “Plasma properties in the plume of a hall thruster cluster,” *Journal of Propulsion and Power*, vol. 20, no. 6, pp. 985–991, 2004.